nature materials

Article

https://doi.org/10.1038/s41563-022-01401-3

Magnetic anisotropy reversal driven by structural symmetry-breaking in monolayer α-$RuCl_3$

Received: 7 March 2022

Accepted: 7 October 2022

Published online: 17 November 2022

Check for updates

Bowen Yang[1,2], Yin Min Goh[3], Suk Hyun Sung[4], Gaihua Ye[5], Sananda Biswas[6], David A. S. Kaib[6], Ramesh Dhakal[7], Shaohua Yan[8], Chenghe Li[8], Shengwei Jiang[9,10], Fangchu Chen[1,2], Hechang Lei[8], Rui He[5], Roser Valentí[6], Stephen M. Winter[7] ✉, Robert Hovden[4,11] ✉ & Adam W. Tsen[1,12] ✉

Layered α-$RuCl_3$ is a promising material to potentially realize the long-sought Kitaev quantum spin liquid with fractionalized excitations. While evidence of this state has been reported under a modest in-plane magnetic field, such behaviour is largely inconsistent with theoretical expectations of spin liquid phases emerging only in out-of-plane fields. These predicted field-induced states have been largely out of reach due to the strong easy-plane anisotropy of bulk crystals, however. We use a combination of tunnelling spectroscopy, magnetotransport, electron diffraction and ab initio calculations to study the layer-dependent magnons, magnetic anisotropy, structure and exchange coupling in atomically thin samples. Due to picoscale distortions, the sign of the average off-diagonal exchange changes in monolayer α-$RuCl_3$, leading to a reversal of spin anisotropy to easy-axis anisotropy, while the Kitaev interaction is concomitantly enhanced. Our work opens the door to the possible exploration of Kitaev physics in the true two-dimensional limit.

The Kitaev model is a celebrated spin-½ model on a two-dimensional honeycomb lattice with bond-dependent Ising interactions[1], that features a highly entangled quantum spin liquid (QSL) ground state, fractionalized Majorana excitations and a series of magnetic-field-induced quantum phase transitions[1–4]. The search for materials realizing the Kitaev model has been an ongoing challenge for over a decade and may potentially lead to applications in fault-tolerant topological quantum computing[5]. Yet the unavoidable presence of non-Kitaev interactions (Heisenberg, off-diagonal, next nearest neighbour and so on) almost always drives the ground state away from the QSL phase, and a careful tuning of the exchange parameters is needed[6–9].

The layered van der Waals material, α-$RuCl_3$, is a particularly promising candidate to realize Kitaev physics[10,11]. Although the ground state is zigzag (ZZ) antiferromagnetic (AFM), this ordering can be suppressed

[1]Institute for Quantum Computing, University of Waterloo, Waterloo, Ontario, Canada. [2]Department of Physics and Astronomy, University of Waterloo, Waterloo, Ontario, Canada. [3]Department of Physics, University of Michigan, Ann Arbor, MI, USA. [4]Department of Materials Science and Engineering, University of Michigan, Ann Arbor, MI, USA. [5]Department of Electrical and Computer Engineering, Texas Tech University, Lubbock, TX, USA. [6]Institut für Theoretische Physik, Goethe-Universität Frankfurt, Frankfurt am Main, Germany. [7]Department of Physics and Center for Functional Materials, Wake Forest University, Winston-Salem, NC, USA. [8]Department of Physics and Beijing Key Laboratory of Opto-electronic Functional Materials & Micro-nano Devices, Renmin University of China, Beijing, China. [9]Department of Physics, Cornell University, Ithaca, NY, USA. [10]Key Laboratory of Artificial Structures and Quantum Control (Ministry of Education), School of Physics and Astronomy, Shanghai Jiao Tong University, Shanghai, China. [11]Applied Physics Program, University of Michigan, Ann Arbor, MI, USA. [12]Department of Chemistry, University of Waterloo, Waterloo, Ontario, Canada. ✉e-mail: winters@wfu.edu; hovden@umich.edu; awtsen@uwaterloo.ca

with the application of an ~6–8 T in-plane magnetic field. The presence of a half-integer thermal quantum Hall effect has been reported in this intermediate phase at low temperature[12,13], while an unusual continuum of magnetic excitations can be seen even without a magnetic field, that persists far above the Néel temperature ($T_N \approx 7$–8 K)[14,15]. Both observations hint at α-$RuCl_3$ being in proximity to a QSL, making it a current subject of intense scrutiny. Yet from a theoretical point of view, a QSL induced by an in-plane field generally cannot be accounted for, as most calculations for α-$RuCl_3$ show Kitaev phases more broadly emerging from an out-of-plane field[4,16–19]. Due to the strong 'easy-plane' magnetic anisotropy of bulk crystals, however, prohibitively high fields above 30 T are required to access such states[20–22].

The strong coupling between the spin, charge and lattice degrees of freedom in α-$RuCl_3$ presents an exciting opportunity to tune its magnetic interactions via changing dimensionality, the aim of the present study. Moreover, pure monolayer systems are in principle expected to more closely realize the Kitaev model compared with their bulk counterparts[23]. To this end, we start by exfoliating α-$RuCl_3$ crystals on oxidized silicon wafers within a nitrogen-filled glove box and identifying their thickness by optical reflection contrast. To confirm that the thinnest flakes are indeed monolayers, we pick up these samples, encapsulate them with monolayer graphene, and transfer them to 10-nm-thick silicon nitride membranes for three-dimensional electron diffraction measurements (Methods). Figure 1a shows an electron diffraction pattern of such a structure. Some of the fundamental Bragg peaks of α-$RuCl_3$ used for determining the monolayer structure are circled, although the graphene peaks (along the thick grey circle) can be seen as well. Measuring relative to the graphene peaks, the in-plane lattice constant of our exfoliated α-$RuCl_3$ is determined to be 5.9981–6.0088 Å, which is consistent with the value for the bulk crystal and thus indicates negligible overall strain[24,25]. By tilting the sample, we can measure the diffraction spots as a function of out-of-plane crystal momentum (k_z). A side-view schematic of the Bragg rod structure for several of the monolayer (1L) α-$RuCl_3$ peaks is shown in Fig. 1b, and the experimental Bragg rod intensities are shown in Fig. 1c as discrete points together with their expected values in solid lines. In particular, the $(1\bar{2}10)$ and $(\bar{1}2\bar{1}0)$ peaks exhibit a reduction of symmetry from the ideal crystal. As the k_z dependence for bilayer (2L) and trilayer (3L) crystals are markedly different (Supplementary Section 1), we can confirm our ability to exfoliate and encapsulate α-$RuCl_3$ crystals down to monolayer thickness.

It has been previously demonstrated that inelastic electron tunnelling spectroscopy (IETS) is a powerful tool to probe for spin waves in ultrathin insulating magnets in the ~1–10 meV range[26,27], the same energy window where various magnetic excitations have been observed in bulk α-$RuCl_3$ (refs. [14,15,25,28–36]). We thus fabricate a series of metal/α-$RuCl_3$/metal tunnel junctions in inert atmosphere to carry out temperature- and magnetic-field-dependent IETS on 1L, 2L and 3L α-$RuCl_3$ samples (Methods). To maximize inelastic electron tunnelling, the metal should possess a sizeable Fermi surface with a substantial density of states[37]. We mostly use ultrathin (<10 nm) T_d-$MoTe_2$ as our metal electrode, although graphene shows qualitatively similar behaviour (Extended Data Fig. 1). A side-view illustration of our device and measurement geometry is shown in Fig. 1d, and a colourized optical image of a representative device is shown in Fig. 1e. Hexagonal boron nitride (hBN) flakes are used as encapsulation layers for protection.

The upper panel of Fig. 1f shows the measured a.c. conductance (dI/dV; I, current; V, voltage) of a 1L tunnel junction at 2 K as a function of the d.c. voltage. Subtle steps in the curve can be seen centred at ~±1 mV, which can be interpreted as increases in the tunnelling conductance when the potential difference across the electrodes reaches the energy of a particular inelastic excitation in α-$RuCl_3$ (refs. [26,27,38]). These can be seen more clearly as peaks in the numerical derivative (d^2I/dV^2) shown in the lower panel of Fig. 1f. To extract the position and shape of the peaks, we fit them to a pair of Lorentzians (blue) on top of a background (grey). The resultant fitting is shown in red, and closely traces the experimental result. We next investigate the dependence of these excitation peaks on temperature across samples of different thicknesses to understand whether they are of magnetic or phononic nature.

Figure 2a shows the normalized and background-subtracted d^2I/dV^2 spectrum for 1L, 2L and 3L devices from 2 K to 10 K in a two-dimensional false-colour plot for positive bias. The trace at the base temperature is overlaid in blue as a reference, while the original temperature-dependent traces (together with the background subtraction procedure) are shown in Extended Data Fig. 2. The mode at ~1 meV appears in all three devices at low temperature and disappears above ~8 K. This is near the T_N measured for the bulk crystal (Extended Data Fig. 3)[25,34], which suggests a magnetic origin. Indeed, phonon features have been observed in this energy range[39], but they persist up to room temperature. Linear spin wave and exact diagonalization calculations based on ab initio studies show a large magnon scattering intensity near 1 meV at the Y and M points[40], while several experiments have reported bulk magnons near this energy[30,31,36]. We have further integrated the previous bulk magnon intensity calculations across the Brillouin zone (Supplementary Section 2), and the resultant spectrum indeed exhibits a peak at ~1 meV. Our observed mode can thus be attributed to the lowest-energy excitation of the ZZ AFM order.

The smaller overall conductance of the thicker 3L device allows us to probe with IETS at higher voltages. Between ~5–10 meV, a broad excitation spectrum is observed that persists up to the highest temperature measured with no apparent discontinuity at T_N. This is consistent with the continuum excitations identified in bulk crystals by Raman and neutron scattering, which have been discussed to be connected to fractionalized and/or incoherent excitations[14,15,28,36]. Our results thus show that such unconventional magnetic signatures persist down to at least 3L samples.

To determine T_N more precisely for different thicknesses, we start by fitting Lorentzians to the low-energy mode in the manner described above. This function is known to be a convolution of the intrinsic spectral weight with a temperature-dependent thermal broadening function, $\chi(V) = \frac{1}{kT}\exp(x)\frac{(x-2)\exp(x)+x+2}{(\exp(x)-1)^3}$, where $x = eV/kT$ (e, electron charge; k, Boltzmann constant; T, temperature), and a temperature-independent instrument broadening function[38]. The latter is negligible for our measurement conditions (Supplementary Section 3). We thus extract the intrinsic peak by deconvolving the fitted experimental curve with χ and integrating the resultant intensity. These values are plotted as a function of temperature in the main panels of Fig. 2b for the three samples. The intercept of a linear fit applied to the data at low temperature yields T_N, values for which are explicitly shown in the inset as a function of sample thickness. The range of T_N measured for high-quality bulk crystals is marked by the grey band. Unlike Heisenberg(-like) magnets obeying the Mermin–Wagner theorem[41], the critical temperature for α-$RuCl_3$ remains essentially unchanged down to a monolayer.

In bulk α-$RuCl_3$, magnons can evolve nonmonotonically with the application of an in-plane magnetic field[28,29,35,36]. For example, the magnons at the Γ point first shift down to lower energies with increasing field, reaching a minimum at ~6–8 T before shifting up. This critical field has been suggested to host an intermediate QSL region (between the ZZ ground state and high-field paramagnetic state)[12,13,36], an idea that remains controversial, in part because theoretical studies have only identified models with QSL phases induced by out-of-plane fields[4,16–19]. Due to the easy-plane anisotropy of bulk crystals, however, an out-of-plane field of ≳30 T is needed to change the magnetic state, rendering such predicted QSLs largely inaccessible[16,20–22,40]. We thus proceed to measure the low-energy magnon for all three sample thicknesses with changing magnetic field. In Fig. 3a, we show 1L, 2L and 3L IETS spectra taken at 2 K for in-plane magnetic field ($B_{\parallel}$) between 0 and 14 T (in 1 T increments), with the traces background subtracted and

https://doi.org/10.1038/s41563-022-01401-3

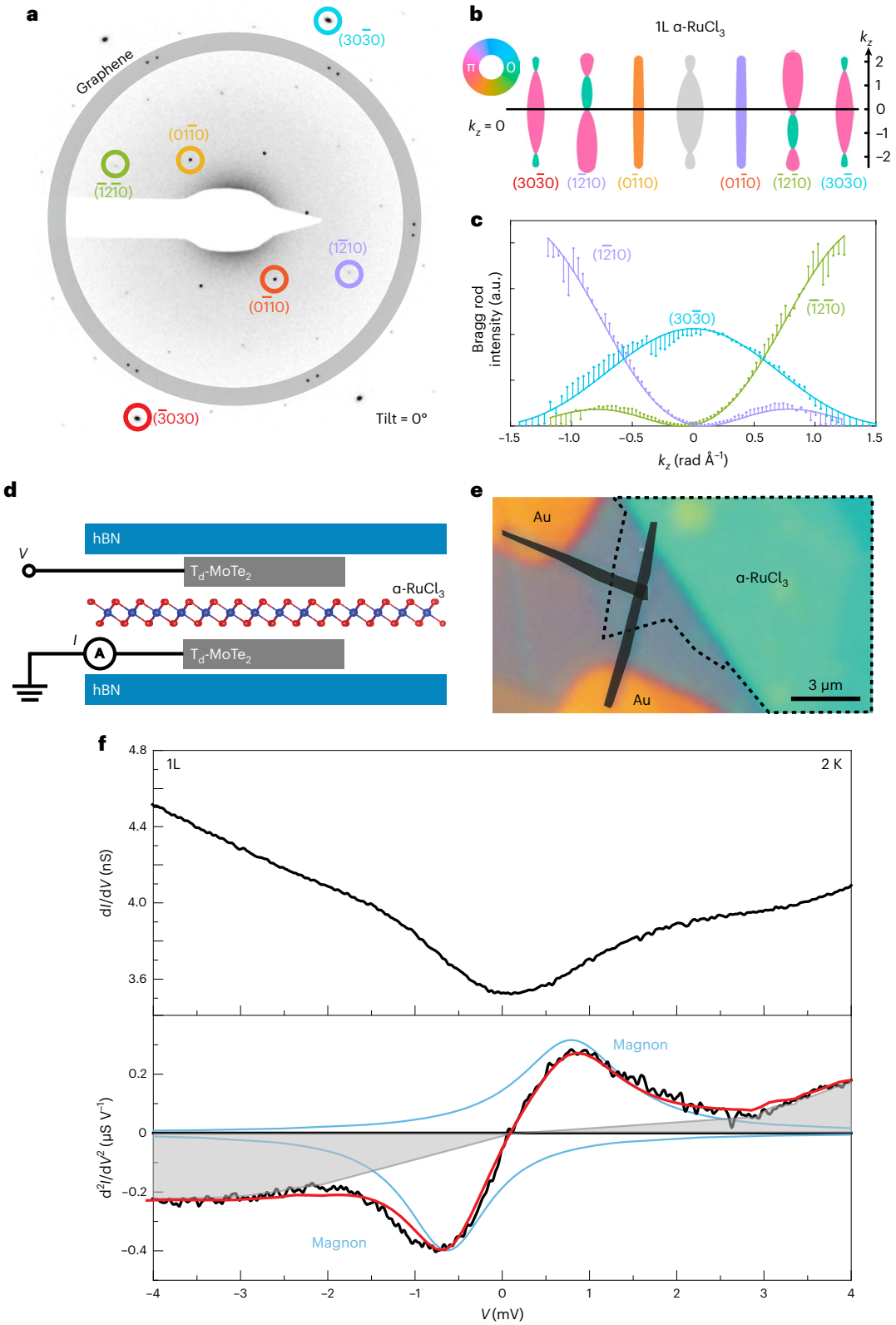

Fig. 1 | Three-dimensional electron diffraction and demonstration of IETS measurements on 1L α-RuCl$_3$. a, Electron diffraction pattern for graphene-encapsulated 1L α-RuCl$_3$ at 0° tilt. Bragg peaks for graphene layers are marked by a thick grey circle. Several α-RuCl$_3$ Bragg peaks selected for analysis are circled. **b**, Schematic of calculated out-of-plane momentum (k_z) dependence for the various Bragg rods of 1L α-RuCl$_3$ chosen in **a**. The thickness and colour indicate the complex magnitude and phase of the structure factor, respectively. **c**, Experimental Bragg intensities (scatter points) for (1$\bar{2}$10), ($\bar{1}$2$\bar{1}$0) and (30$\bar{3}$0) peaks, plotted as a function of k_z, show great agreement with a fitted kinematic model (lines) of 1L α-RuCl$_3$. Vertical lines are the residuals from fitting the kinematic model (solid lines) to experimental data (scatter points). **d**, Side-view schematic of an IETS device with vertical T$_d$-MoTe$_2$ contacts to few-layer α-RuCl$_3$. **e**, Colourized optical image of a 1L α-RuCl$_3$ device. Black shaded areas represent T$_d$-MoTe$_2$, and dashed lines outline a α-RuCl$_3$ flake. **f**, Representative IETS results for 1L α-RuCl$_3$ taken at 2 K. The upper panel shows the a.c. tunnelling conductance dI/dV as a function of applied d.c. voltage, showing subtle steps due to magnon excitations at both positive and negative voltages. The lower panel shows the numerical derivative (black trace) of the experimental dI/dV curve, d^2I/dV^2, together with results from the fitting (grey, background; blue lines, Lorentzian fits to magnon peaks; red, overall fit).

https://doi.org/10.1038/s41563-022-01401-3

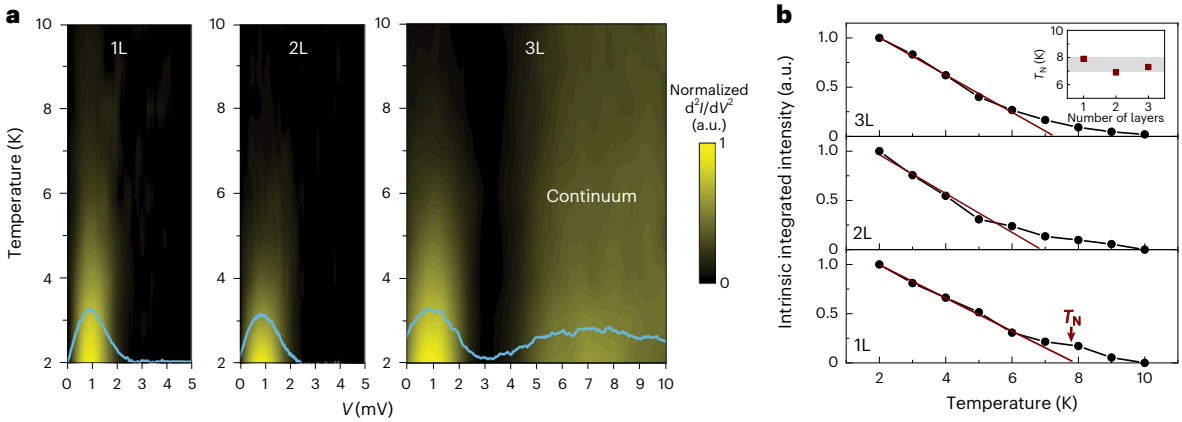

Fig. 2 | Temperature-dependent IETS of few-layer α-$RuCl_3$. a, False-colour plot of normalized and background-subtracted d^2I/dV^2 spectra for 1L, 2L and 3L α-$RuCl_3$ from 2 K to 10 K at positive d.c. bias. The trace at 2 K for each thickness is overlaid in blue. A broad excitation between ~5 meV to ~10 meV is observed for 3L and attributed to the magnon continuum. **b**, Intrinsic integrated intensity of ~1 meV magnon for 1L, 2L and 3L α-$RuCl_3$ at each temperature. The data points from 2 K to 6 K are utilized for linear fittings (red lines), whose *x* intercepts yield T_N. The inset shows the thickness-dependent T_N for 1L, 2L and 3L α-$RuCl_3$, all of which fall in the range of 7–8 K (grey band), which corresponds to the range reported for high-quality bulk crystals.

offset for clarity. The original data without background subtraction can be found in Extended Data Fig. 4a. To determine the magnon energies more quantitatively, we performed a Lorentzian fit for each trace, and the extracted peak positions are marked by the inverted grey triangle in Fig. 3a and plotted explicitly in Fig. 3b with changing $B_{\parallel}$. The 2L and 3L samples show qualitatively similar characteristics—with increasing field, the magnon energy first decreases and then increases, although the field at which the minimum energy occurs appears to be slightly larger for 2L. These results can be compared with calculations for the momentum-integrated bulk magnon intensity with changing in-plane magnetic field (Supplementary Section 2). In addition, we observe that the high-energy continuum feature for 3L also changes with in-plane field (Extended Data Fig. 5), which is consistent with its magnetic origin.

By contrast, the magnon for 1L is essentially unchanged with a magnetic field up to 14 T, which suggests that the critical in-plane field necessary to drive the monolayer out of the ZZ state is pushed to a substantially higher value. This trend is captured by the thick blue line in Fig. 3b. We further note that the observed magnon stiffening for 1L appears to be independent of whether the field is directed along either of the two in-plane crystalline axes (Supplementary Section 4).

Figure 3c shows the out-of-plane field dependence ($B_{\perp}$) of the IETS spectra (Extended Data Fig. 4b shows original data without background subtraction). Here, an opposite trend is observed with changing thickness. The 3L has the stiffest response, consistent with the result for bulk crystals[34], while the low-energy peak position for both 2L and 1L exhibit more curvature with field. Interestingly, a secondary peak at higher energy also develops for the latter samples at finite fields. We have fit all the observed peaks to Lorentzians, and the positions are marked in Fig. 3c by grey and magenta inverted triangles and plotted explicitly in Fig. 3d as a function of $B_{\perp}$. At high fields, the secondary peaks appear to shift with field at roughly twice the rate compared with the low-energy magnon, suggesting that they may originate from two-magnon excitation[28,29,36,40]. The larger curvature exhibited by this higher-energy mode also allows us to clearly identify the critical field for which the energy is minimum—it shifts to higher values with increasing thickness. This trend is captured by the thick orange line in Fig. 3d and is consistent with the extremely large out-of-plane critical field expected for the bulk crystal. Taken together, the results of Fig. 3 suggest that the magnetic anisotropy is reversed from easy-plane anisotropy for bulk crystals to easy-axis (out-of-plane) anisotropy for 1L α-$RuCl_3$. Such a change is striking; however, we must ascertain whether it is intrinsic to monolayer samples or a result of proximity to the T_d-$MoTe_2$, a system with strong spin–orbit coupling.

To address this issue, we have fabricated an ultrashort two-terminal device for 1L α-$RuCl_3$ with both few-layer graphene electrodes and top and bottom gates to investigate the field dependence of lateral transport. A colourized scanning electron microscope image and side-view schematic of the device are shown in Fig. 4a. The sample is only in contact with hBN across the channel (length, ~300 nm). Figure 4b shows the d.c. current–voltage dependence at base temperature for different gate values. Due to the insulating nature of α-$RuCl_3$, the sample shows a measurable current only at low bias when large positive gate voltages are applied (electron doping). In the most conductive state (top gate voltage V_{TG} = 9 V, bottom gate voltage V_{BG} = 6 V), we have measured the a.c. conductance upon sweeping the magnetic field (both in plane and out of plane) continuously, and the results are plotted in Fig. 4c for several different temperatures. Overall, there is very little change with the in-plane field, consistent with this field direction being along the hard axis. By contrast, there is a larger change when the field is applied along the easy axis, out of plane. Moreover, a marked kink can be seen in the magnetoconductance at $B_{\perp} \approx 6.5$ T at low temperatures. This coincides with the critical field for the two-magnon feature measured by IETS. Upon raising the temperature, the kink gradually disappears above T_N. These results indicate that the magnetic anisotropy reversal in monolayer α-$RuCl_3$ is likely of intrinsic origin as opposed to proximal contact with T_d-$MoTe_2$.

It is well understood that spin moments in α-$RuCl_3$ are strongly coupled to the charge and lattice degrees of freedom[9,42–45]. In particular, electron transfer effects have been previously observed in various two-dimensional heterostructures incorporating α-$RuCl_3$ (ref. [46]). Theoretical analysis shows that the magnetic anisotropy is unlikely to be affected by doping, however[23]. Thus, a more probable cause is that the structure of 1L α-$RuCl_3$ deviates from that of the bulk crystal. To investigate whether this is the case, we again turn to electron diffraction measurements performed on the monolayer sample. By carefully fitting the k_z dependence for the various Bragg peaks, we observe three primary distortions of the honeycomb lattice of edge-sharing $RuCl_6$ octahedra (Supplementary Section 1), which are illustrated in Fig. 5a. First, there is an out-of-plane buckling of the Ru atoms, $\Delta\zeta_{Ru}$, discernable from the asymmetric $(01\bar{1}0)$ and $(0\bar{1}10)$ Bragg rods shown in Fig. 5b. Due to negligible overall strain in the lattice (as described in the discussion of Fig. 1a), the in-plane distortion of Ru should not be substantial. Second, there is a change in the *c*-axis position Cl atoms relative to the Ru atoms, λ_{Cl}, as well as a third in-plane distortion of the Cl atoms that are opposite for the top and bottom sublayers, Δr_{Cl}. A table summarizing the experimentally bounded values for these three distortions

https://doi.org/10.1038/s41563-022-01401-3

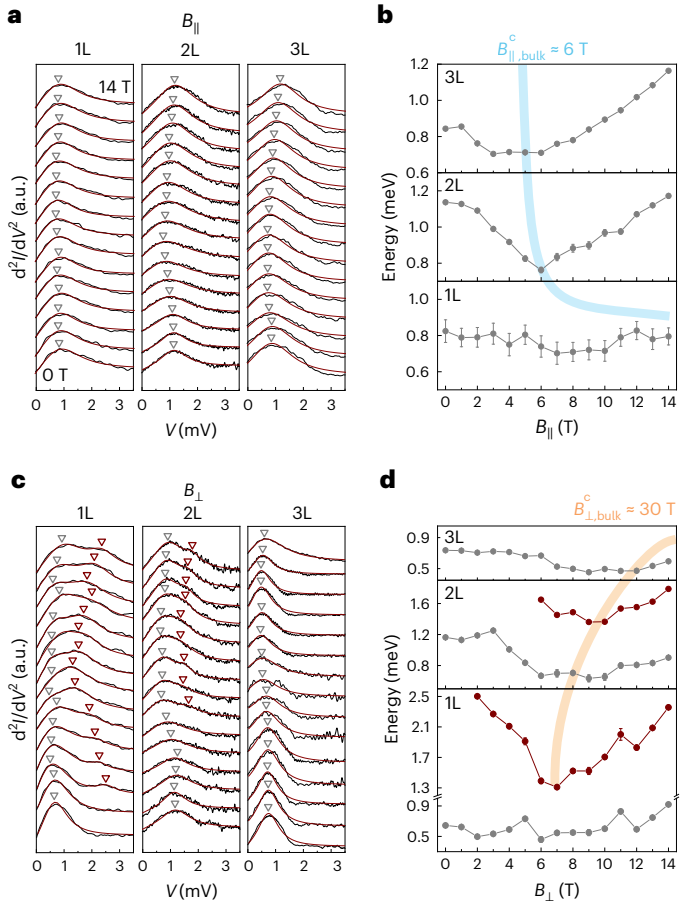

Fig. 3 | Magnetic-field-dependent IETS on few-layer α-RuCl$_3$. a–d, The 1L, 2L and 3L α-RuCl$_3$ spectra (black lines) with changing $B_{\parallel}$ (**a**) and $B_{\perp}$ (**c**) from 0 T to 14 T in 1 T increments and offset for clarity. Lorentzian fitting and background subtraction is performed for each d^2I/dV^2 trace (red lines). The extracted peak positions are marked by the inverted grey and magenta triangles and plotted explicitly as a function of $B_{\parallel}$ (**b**) and $B_{\perp}$ (**d**). Grey points are results for low-energy magnons, and magenta points are secondary peaks at higher energy, which correspond to two-magnon scattering at high fields. The thick blue and orange lines capture trends in the changing critical field with thickness, for $B_{\parallel}$ and $B_{\perp}$, respectively. Error bars represent standard errors of the peak position obtained from Lorentzian fitting of the IETS spectra. In most cases, the size of the data point is larger than the error bars.

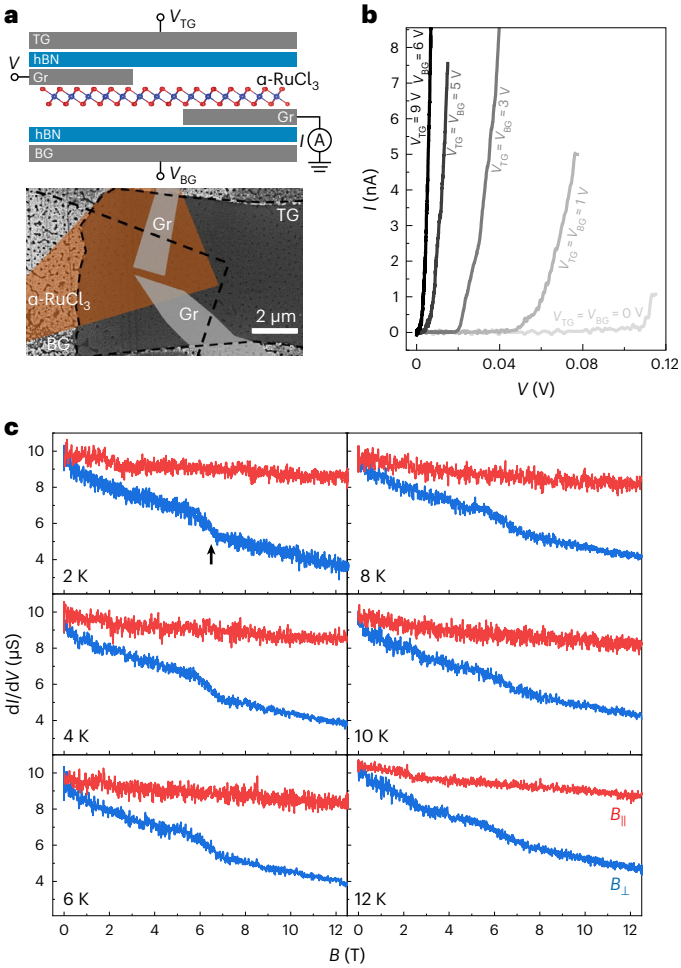

Fig. 4 | Lateral magnetotransport measurement on 1L α-RuCl$_3$ with dual gates. a, Side-view schematic (top) and colourized scanning electron microscopy image (bottom) of device with channel length of ~300 nm (TG, top gate; BG, bottom gate; Gr, graphene). Dashed lines outline the top and bottom gates. **b**, Curves of the d.c. current–voltage characteristics at 2 K taken with various gate voltages. **c**, The a.c. conductance at 20 mV d.c. bias, 9 V top gate and 6 V bottom gate with changing $B_{\parallel}$ (red) and $B_{\perp}$ (blue) from 2 K to 12 K. The magnetoconductance has a larger change overall with $B_{\perp}$ and a marked kink at $B_{\perp} \approx 6.5$ T (marked with a black arrow) that gradually disappears above $T_N \approx 8$K.

is shown in Fig. 5a. Similar distortions have been previously observed on the surfaces of exfoliated α-RuCl$_3$ flakes and have been attributed to Cl vacancies despite preparation in an inert atmosphere[47]. Our results suggest that they may instead be intrinsic to the monolayer when interlayer coupling is absent; although, diffraction provides a precise measure of the average crystal structure and distortions, but is much less sensitive to real-space fluctuations.

The reversal of magnetic anisotropy for 1L α-RuCl$_3$ signifies a modification of the spin Hamiltonian $\mathcal{H} = \sum_{<i,j>} \mathbf{S}_i \cdot \mathbf{M}_{ij} \cdot \mathbf{S}_j$ due to the observed distortions, where $\mathbf{S}_{i(j)}$ is the spin of Ru site $i(j)$. For coplanar Ru, the matrix $\mathbf{M}$ (for the z bond) can be expressed as $\begin{pmatrix} J & \Gamma & \Gamma' \\ \Gamma & J & \Gamma' \\ \Gamma' & \Gamma' & J+K \end{pmatrix}$ for nearest-neighbour interactions, where J, K and Γ (Γ') refer to the Heisenberg, Kitaev and off-diagonal coupling terms, respectively, although a third neighbour Heisenberg term J_3 is expected to contribute as well. With Ru buckling, the symmetry of $\mathbf{M}$ is lowered to $\begin{pmatrix} J_x & \Gamma_{xy} & \Gamma_{xz} \\ \Gamma_{xy} & J_y & \Gamma_{yz} \\ \Gamma_{xz} & \Gamma_{yz} & J_z \end{pmatrix}$, where the Kitaev coupling is now defined by $K = J_z - (J_x + J_y)/2$. The sense of the exchange anisotropy is determined by the sum of the off-diagonal couplings $\Sigma\Gamma = \Gamma_{xy} + \Gamma_{xz} + \Gamma_{yz}$ with positive (negative) values indicative of easy-plane (easy-axis) anisotropy. In the bulk, the large out-of-plane critical field stems primarily from the large off-diagonal $\Gamma > 0$ term, which is the main competitor to the Kitaev interaction.

To correlate the distortions with microscopic interactions, we performed ab initio calculations of the spin Hamiltonian for a range of distortions and evaluated the classical ground state magnetic order, schematics of which are shown in the upper part of Fig. 5c (Methods and Supplementary Section 5). The results are shown in the lower panels of Fig. 5c as two sets of false-colour plots for $\Sigma\Gamma$ as a function of the Cl distortions. The left (right) panel is calculated without (with) Ru buckling. The plots also map out a phase diagram for the magnetic ordering. Regions where classical striped (Str), ZZ and ferromagnetic (FM) phases compete have been theorized to realize a QSL state in the bulk[7,16]. The position of bulk α-RuCl$_3$ is marked by the black circle in the left panel of Fig. 5c (refs. [24,25]), while the dashed rectangle in the right panel outlines our 1L α-RuCl$_3$ within the error limits of electron diffraction. We have also used density functional theory to calculate

https://doi.org/10.1038/s41563-022-01401-3

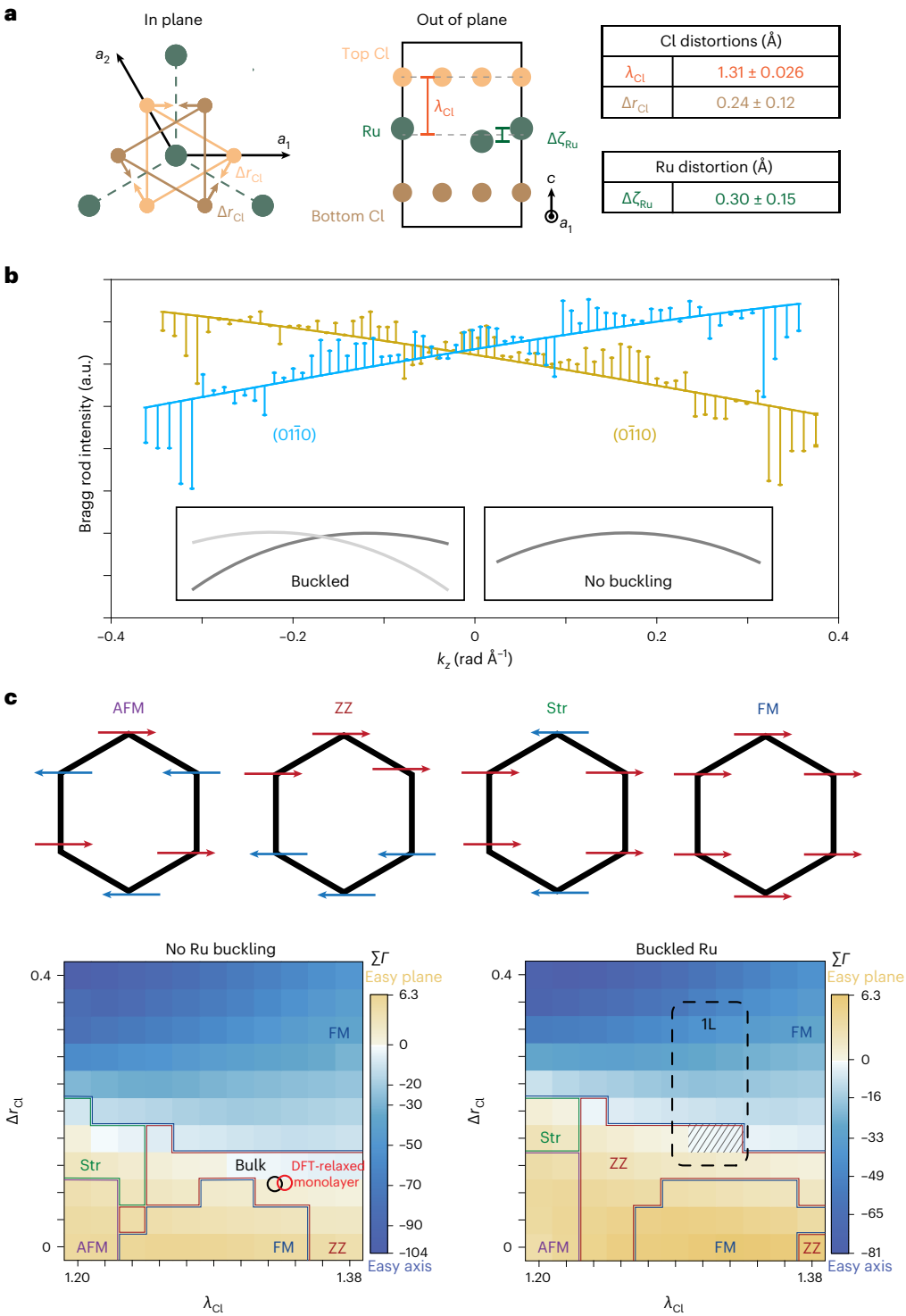

Fig. 5 | Three primary distortions of 1L α-$RuCl_3$ and magnetic phase diagram. **a**, Schematic illustration of three distortions ($\Delta\zeta_{Ru}$, λ_{Cl} and Δr_{Cl}; left) and summary of the values determined by three-dimensional electron diffraction measurements (right). $\vec{a}_1 = a(1,0)$ and $\vec{a}_2 = a\left(-\frac{1}{2}, \frac{\sqrt{3}}{2}\right)$ are the lattice vectors of α-$RuCl_3$, where a = 5.979 Å is the lattice constant. **b**, Asymmetric (01$\bar{1}$0) and (0$\bar{1}$10) Bragg rod intensities versus k_z indicate out-of-plane Ru buckling. The inset shows a schematic for the two Bragg rods with and without Ru buckling. Vertical lines are residuals of fit. **c**, The lower panel shows a magnetic phase diagram determined by ab initio calculations of $\Sigma\Gamma$ as a function of the Cl distortions without Ru buckling ($\Delta\zeta_{Ru}$ = 0 Å, left) and with Ru buckling ($\Delta\zeta_{Ru}$ = 0.3 Å, right). Yellow (blue) regions correspond to easy-plane (easy-axis) magnetic anisotropy. Positions for the experimental bulk structure and density functional theory (DFT)-relaxed monolayer are circled in the case of no buckling. The dashed rectangle in the right panel outlines our 1L α-$RuCl_3$ within the error limits of electron diffraction. The hashed area marks a region, within the rectangle, where the ZZ magnetic anisotropy has flipped to out of plane (easy axis). The upper panel shows schematics of the various classical magnetic orders in the phase diagram.

the relaxed structure of the free-standing monolayer (Methods and Supplementary Section 6), which appears near that of the experimental bulk structure and does not exhibit Ru buckling (red circle, left panel). While the precise microscopic origin of the observed buckling is left as an open question, we can effectively rule out the effect of the substrate as well as a high density of Cl vacancies (Supplementary

Table 1 | Summary of the estimated exchange couplings (meV) for 1L and bulk α-$RuCl_3$

	J	K	Γ	Γ'
No buckling (bulk α-$RuCl_3$)	−3.3	−6.4	3.6	−0.7

	J_x	J_y	J_z	Γ_{xy}	Γ_{yz}	Γ_{xz}
Ru buckling (1L α-$RuCl_3$)	−3.1	−4.0	−11.8	2.3	−4.5	1.4

The Heisenberg (J), Kitaev (K) and off-diagonal (Γ,Γ') coupling terms for bulk α-$RuCl_3$ with no buckling are listed in the upper rows of the table. The elements of the matrix of exchange coupling terms, $\begin{pmatrix} J_x & \Gamma_{xy} & \Gamma_{xz} \\ \Gamma_{xy} & J_y & \Gamma_{yz} \\ \Gamma_{xz} & \Gamma_{yz} & J_z \end{pmatrix}$, are listed in the lower rows for 1L α-$RuCl_3$ with Ru buckling.

Section 6). The distortions collectively increase (decrease) the cation–cation (cation–anion) distance, creating more-favourable Coulomb interactions.

The hashed area in the phase diagram on the right of Fig. 5c marks a region within the ZZ state (that is also within the dashed rectangle) where the magnetic anisotropy has flipped to be out of plane, which lies on the border of FM order. To narrow the 1L phase boundary further, we performed magnetic circular dichroism measurements on 1L α-$RuCl_3$ to measure the out-of-plane magnetization, and the results are inconsistent with a FM phase with easy-axis anisotropy (Methods and Extended Data Fig. 6), indicating that our monolayers most likely retain the ZZ configuration and possess a value of $\Sigma\Gamma$ that is small and negative (and hence reside in the hashed region). The various exchange terms estimated for this region as well as for the bulk structure are summarized in Table 1. We thus see that the anisotropy reversal in monolayer samples is largely driven by the in-plane Cl distortion, which suppresses and reverses the off-diagonal exchange. Similar analysis of the g-factor supports this conclusion (Supplementary Section 5). The 1L α-$RuCl_3$ appears to be near a transition to out-of-plane FM ordering as a result. Proximity to this phase boundary necessarily leads to greater spin frustration and an enhanced Kitaev interaction. Specifically, we calculate $K = J_z - (J_x + J_y)/2 = -8.25$ meV for the hashed region, larger than that for the bulk. Due to out-of-plane Cl compression relative to the bulk structure, 1L α-$RuCl_3$ also lies closer to the region where Str, ZZ and out-of-plane FM phases compete.

In conclusion, our tunnelling measurements on two-dimensional α-$RuCl_3$ reveal the presence of single-magnon and/or two-magnon modes down to the monolayer limit, and a magnon continuum in 3L α-$RuCl_3$. The evolution of magnons with magnetic field indicates a clear change in the magnetic anisotropy from easy plane to easy axis in monolayer form that is supported by magnetotransport measurements in a gated lateral geometry. Three-dimensional electron diffraction shows that 1L α-$RuCl_3$ possesses several structural distortions, among which an in-plane Cl distortion predominantly drives the anisotropy reversal. This is supported by ab initio calculations, which are also used to extract a microscopic spin Hamiltonian and distortion-dependent magnetic phase diagram. Relative to the bulk, the ground state of 1L α-$RuCl_3$ has a larger Kitaev interaction and lies in closer proximity to the intersection of several competing spin orders. Furthermore, while a field-induced QSL for in-plane fields in bulk α-$RuCl_3$ remains a subject of intense debate, a variety of theoretical works have predicted QSL phases for out-of-plane fields that have hitherto been inaccessible due to the large easy-plane anisotropy[4,16–19]. Such states may now be potentially realized for monolayer samples. Our results demonstrate the importance of dimensionality in tuning magnetism in strongly correlated spin systems and pave the way for versatile experimental knobs used for two-dimensional materials (electric field, doping, strain and so on) to further modify the magnetic order in atomically thin α-$RuCl_3$.

Online content

Any methods, additional references, Nature Research reporting summaries, source data, extended data, supplementary information, acknowledgements, peer review information; details of author contributions and competing interests; and statements of data and code availability are available at https://doi.org/10.1038/s41563-022-01401-3.

References

1. Kitaev, A. Anyons in an exactly solved model and beyond. *Ann. Phys.* **321**, 2–111 (2006).
2. Patel, N. D. & Trivedi, N. Magnetic field-induced intermediate quantum spin liquid with a spinon Fermi surface. *Proc. Natl Acad. Sci. USA* **116**, 12199–12203 (2019).
3. Hickey, C. & Trebst, S. Emergence of a field-driven $U(1)$ spin liquid in the Kitaev honeycomb model. *Nat. Commun.* **10**, 530 (2019).
4. Kaib, D. A. S., Winter, S. M. & Valentí, R. Kitaev honeycomb models in magnetic fields: dynamical response and dual models. *Phys. Rev. B* **100**, 144445 (2019).
5. Freedman, M. H., Kitaev, A., Larsen, M. J. & Wang, Z. Topological quantum computation. *Bull. Am. Math. Soc.* **40**, 31–38 (2003).
6. Chaloupka, J., Jackeli, G. & Khaliullin, G. Zigzag magnetic order in the iridium oxide Na_2IrO_3. *Phys. Rev. Lett.* **110**, 097204 (2013).
7. Rau, J. G., Lee, E. K. H. & Kee, H. Y. Generic spin model for the honeycomb iridates beyond the Kitaev limit. *Phys. Rev. Lett.* **112**, 077204 (2014).
8. Winter, S. M., Li, Y., Jeschke, H. O. & Valentí, R. Challenges in design of Kitaev materials: magnetic interactions from competing energy scales. *Phys. Rev. B* **93**, 214431 (2016).
9. Winter, S. M. et al. Models and materials for generalized Kitaev magnetism. *J. Phys. Condens. Matter* **29**, 493002 (2017).
10. Plumb, K. W. et al. *α*–$RuCl_3$: a spin-orbit assisted Mott insulator on a honeycomb lattice. *Phys. Rev. B* **90**, 041112 (2014).
11. Takagi, H., Takayama, T., Jackeli, G., Khaliullin, G. & Nagler, S. E. Concept and realization of Kitaev quantum spin liquids. *Nat. Rev. Phys.* **1**, 264–280 (2019).
12. Kasahara, Y. et al. Majorana quantization and half-integer thermal quantum Hall effect in a Kitaev spin liquid. *Nature* **559**, 227–231 (2018).
13. Yokoi, T. et al. Half-integer quantized anomalous thermal Hall effect in the Kitaev material candidate α-$RuCl_3$. *Science* **373**, 568–572 (2021).
14. Sandilands, L. J., Tian, Y., Plumb, K. W., Kim, Y. J. & Burch, K. S. Scattering continuum and possible fractionalized excitations in *α*–$RuCl_3$. *Phys. Rev. Lett.* **114**, 147201 (2015).
15. Banerjee, A. et al. Neutron scattering in the proximate quantum spin liquid α-$RuCl_3$. *Science* **356**, 1055–1059 (2017).
16. Yadav, R. et al. Kitaev exchange and field-induced quantum spin-liquid states in honeycomb *α*-$RuCl_3$. *Sci. Rep.* **6**, 37925 (2016).
17. Jiang, Y. F., Devereaux, T. P. & Jiang, H. C. Field-induced quantum spin liquid in the Kitaev-Heisenberg model and its relation to *α*–$RuCl_3$. *Phys. Rev. B* **100**, 165123 (2019).
18. Chern, L. E., Kaneko, R., Lee, H. Y. & Kim, Y. B. Magnetic field induced competing phases in spin-orbital entangled Kitaev magnets. *Phys. Rev. Res.* **2**, 013014 (2020).
19. Zhang, S. S., Halász, G. B. & Batista, C. D. Theory of the Kitaev model in a [111] magnetic field. *Nat. Commun.* **13**, 399 (2022).
20. Li, H. et al. Identification of magnetic interactions and high-field quantum spin liquid in *α*-$RuCl_3$. *Nat. Commun.* **12**, 4007 (2021).
21. Modic, K. A. et al. Scale-invariant magnetic anisotropy in $RuCl_3$ at high magnetic fields. *Nat. Phys.* **17**, 240–244 (2020).
22. Zhou, X.-G. et al. Intermediate quantum spin liquid phase in the Kitaev material α-$RuCl_3$ under high magnetic fields up to 100 T. Preprint at https://arxiv.org/abs/2201.04597 (2022).

23. Biswas, S., Li, Y., Winter, S. M., Knolle, J. & Valentí, R. Electronic properties of α–$RuCl_3$ in proximity to graphene. *Phys. Rev. Lett.* **123**, 237201 (2019).
24. Park, S.-Y. et al. Emergence of the isotropic Kitaev honeycomb lattice with two-dimensional Ising universality in α-$RuCl_3$. Preprint at https://arxiv.org/abs/1609.05690 (2016).
25. Cao, H. B. et al. Low-temperature crystal and magnetic structure of α–$RuCl_3$. *Phys. Rev. B* **93**, 134423 (2016).
26. Klein, D. R. et al. Probing magnetism in 2D van der Waals crystalline insulators via electron tunneling. *Science* **360**, 1218–1222 (2018).
27. Kim, H. H. et al. Evolution of interlayer and intralayer magnetism in three atomically thin chromium trihalides. *Proc. Natl Acad. Sci. USA* **166**, 11131–11136 (2019).
28. Sahasrabudhe, A. et al. High-field quantum disordered state in α–$RuCl_3$ spin flips bound states and a multi-particle continuum. *Phys. Rev. B* **101**, 140410 (2020).
29. Ponomaryov, A. N. et al. Nature of magnetic excitations in the high-field phase of α–$RuCl_3$. *Phys. Rev. Lett.* **125**, 037202 (2020).
30. Banerjee, A. et al. Proximate Kitaev quantum spin liquid behaviour in a honeycomb magnet. *Nat. Mater.* **15**, 733–740 (2016).
31. Ran, K. et al. Spin-wave excitations evidencing the Kitaev interaction in single crystalline α–$RuCl_3$. *Phys. Rev. Lett.* **118**, 107203 (2017).
32. Wang, Z. et al. Magnetic excitations and continuum of a possibly field-induced quantum spin liquid in α–$RuCl_3$. *Phys. Rev. Lett.* **119**, 227202 (2017).
33. Wu, L. et al. Field evolution of magnons in α–$RuCl_3$ by high-resolution polarized terahertz spectroscopy. *Phys. Rev. B* **98**, 094425 (2018).
34. Shi, L. Y. et al. Field-induced magnon excitation and in-gap absorption in the Kitaev candidate $RuCl_3$. *Phys. Rev. B* **98**, 094414 (2018).
35. Balz, C. et al. Finite field regime for a quantum spin liquid in α–$RuCl_3$. *Phys. Rev. B* **100**, 60405 (2019).
36. Wulferding, D. et al. Magnon bound states versus anyonic Majorana excitations in the Kitaev honeycomb magnet α-$RuCl_3$. *Nat. Commun.* **11**, 1603 (2020).
37. Harada, T. et al. Spin-filter tunnel junction with matched Fermi surfaces. *Phys. Rev. Lett.* **109**, 076602 (2012).
38. Lambe, J. & Jaklevic, R. C. Molecular vibration spectra by inelastic electron tunneling. *Phys. Rev.* **165**, 821–832 (1968).
39. Li, H. et al. Giant phonon anomalies in the proximate Kitaev quantum spin liquid α-$RuCl_3$. *Nat. Commun.* **12**, 77203 (2021).
40. Winter, S. M. et al. Breakdown of magnons in a strongly spin-orbital coupled magnet. *Nat. Commun.* **8**, 1152 (2017).
41. Mermin, N. D. & Wagner, H. Absence of ferromagnetism or antiferromagnetism in one- or two-dimensional isotropic Heisenberg models. *Phys. Rev. Lett.* **17**, 1133–1136 (1966).
42. Yadav, R., Rachel, S., Hozoi, L., Van Den Brink, J. & Jackeli, G. Strain- and pressure-tuned magnetic interactions in honeycomb Kitaev materials. *Phys. Rev. B* **98**, 121107(R) (2018).
43. Kaib, D. A. S., Biswas, S., Riedl, K., Winter, S. M. & Valentí, R. Magnetoelastic coupling and effects of uniaxial strain in α–$RuCl_3$ from first principles. *Phys. Rev. B* **103**, L140402 (2021).
44. Bachus, S. et al. Thermodynamic perspective on field-induced behavior of α–$RuCl_3$. *Phys. Rev. Lett.* **125**, 097203 (2020).
45. Maksimov, P. A. & Chernyshev, A. L. Rethinking α–$RuCl_3$. *Phys. Rev. Res.* **2**, 033011 (2020).
46. Wang, Y. et al. Modulation doping via a two-dimensional atomic crystalline acceptor. *Nano Lett.* **20**, 8446–8452 (2020).
47. Dai, Z. et al. Crystal structure reconstruction in the surface monolayer of the quantum spin liquid candidate α-$RuCl_3$. *2D Mater.* **7**, 035004 (2020).

Methods

Crystal synthesis

For α-$RuCl_3$, α-$RuCl_3$ single crystals were grown using the chemical vapour transport method. First, commercial $RuCl_3$ powder was dehydrated at 473 K for 12 hours in a dynamic vacuum. Then, dry $RuCl_3$ powder was put into a silica tube with a length of 20 cm. The tube was evacuated down to 10^{-2} Pa and sealed under vacuum. The source zone temperature was increased to 923 K, and the growth zone to 823 K. The growth period was about seven days, and then the furnace was cooled naturally. Shiny, black, plate-like single crystals of α-$RuCl_3$ were obtained.

For T_d-$MoTe_2$, 1T′-$MoTe_2$ (room temperature phase) single crystals were grown by the flux method using Te as a solvent. Mo (Alfa Aesar, 99.9%) and Te (Alfa Aesar, 99.99%) powders were ground and placed into alumina crucibles in a ratio of 1:25 and sealed in a quartz ampoule. After the quartz ampoule was heated to 1,050 °C and held for two days, the ampoule was slowly cooled to 900 °C over 120 hours and centrifuged. Shiny and plate-like crystals with lateral dimensions of up to several millimetres were obtained.

Device fabrication

The α-$RuCl_3$, graphite/graphene (HQ Graphene), hBN (HQ Graphene) and 1T′-$MoTe_2$ were exfoliated on polydimethylsiloxane-based gel (Gel-Pak) within a nitrogen-filled glove box ($P_{O_2}, P_{H_2O} < 0.1$ ppm, where P is partial pressure). Contact electrodes (17 nm Au/3 nm Ti) and wire-bonding pads (40 nm Au/5 nm Ti) were prepatterned by conventional photolithography and electron-beam deposition. Device heterostructures for IETS (hBN/$MoTe_2$/α-$RuCl_3$/$MoTe_2$/hBN), gated lateral transport (Gr/hBN/Gr/1L α-$RuCl_3$/Gr/hBN/Gr) and electron diffraction (1L Gr/1L α-$RuCl_3$/1L Gr) samples were sequentially stacked by polycarbonate films at 90 °C in the glove box. To prevent electrical breakdown of the atomically thin α-$RuCl_3$, the current should be minimized in IETS measurements, and so the junction area was kept small (around 0.3 μm^2, 1.5 μm^2 and 5 μm^2 for 1L, 2L and 3L α-$RuCl_3$, respectively).

Magnetotransport measurements

Magnetotransport measurements were mostly performed in a superconducting magnet He4 cryostat (base temperature, 1.4 K; magnetic field limit, 14 T). A superconducting magnet He3 cryostat (base temperature, 0.3 K; magnetic field limit, 12 T) was used for an IETS device with Gr contacts. Both set-ups have a single-axis rotator for the sample stage. The d.c. measurements were performed using a Keithley 2450 source measure unit. The d.c. + a.c. measurements were performed using a combination of a Keithley 2450 source measure unit and SRS 830/860 lock-in amplifiers.

Three-dimensional electron diffraction measurements

Acquiring three-dimensional electron diffraction patterns was accomplished by tilting the specimen over a range of angles relative to the incident beam to provide slices through the reciprocal structure. Selected area electron diffraction (SAED) patterns were acquired on the TFS Talos F200X G2 operating at 80 keV with a transmission electron microscopy holder tilting the sample from +35° to −35° in 1° increments. An accelerating voltage of 80 keV was chosen to minimize beam-induced damage to the two-dimensional material. A 0.75 μm selected area electron diffraction aperture was centred over the same sample region throughout the tilt series acquisition. Each selected area electron diffraction image in the tilt series is first background subtracted and aligned to a common centre. Diffraction spots pertaining to α-$RuCl_3$ at every specimen tilt were characterized by fitting a four-parameter two-dimensional Gaussian to a windowed region about each peak. The integrated diffraction peak intensity was then calculated and plotted against k_z for curve fitting with the kinematic model.

Raman spectroscopy

Raman spectroscopy was carried out at room temperature using a 532 nm excitation laser in a backscattering geometry with a beam spot size of ~1 μm. The laser power was kept at ~0.1 μW to minimize the local heating effect. The scattered light was dispersed by a Horiba LabRAM HR Evolution Raman Microscope system and detected by a thermoelectric cooled CCD (charge-coupled device) camera. The hBN-encapsulated α-$RuCl_3$ flakes were mounted on a rotatable stage and measured at every 10°.

Magnetic circular dichroism

The magnetization of hBN-encapsulated 1L α-$RuCl_3$ flakes was characterized by magnetic circular dichroism microscopy in a superconducting magnet He4 cryostat (AttoDry1000) with out-of-plane magnetic field. A diode laser at 410 nm with an optical power of ~10 μW was focused onto a submicrometre spot on the flakes using an objective with a numerical aperture of 0.8. The optical excitation was modulated by a photoelastic modulator at ~50 kHz for left and right circular polarization. The laser light reflected from α-$RuCl_3$ was collected by the same objective and then detected by a photodiode. The magnetic circular dichroism signal is defined as the ratio of the modulated signal (measured by a lock-in amplifier) to the total reflected light power (measured by a d.c. voltmeter).

Ab initio calculations

Magnetic couplings. In order to estimate the magnetic couplings, we employed the exact diagonalization method outlined in refs. [8,48]. Hopping integrals, crystal field tensors and spin–orbit coupling in the basis of the five Ru 4d orbitals were first computed for each structure using the density functional theory package FPLO (ref. [49]) at the fully relativistic generalized gradient approximated (Perdew–Burke–Ernzerhof) level. For structures without Ru buckling, we employed an idealized monolayer structure with $P312/m$ symmetry and a large vacuum gap between monolayers. The in-plane lattice constant was set to 5.979 Å, which is consistent with the results of electron diffraction. To simulate the Ru buckling, we repeated the calculations with $\Delta\zeta_{Ru} = 0.3$ Å, representing the best fit from electron diffraction (formally lowering the symmetry to $P3$). For each structure, the computed one-particle terms, $H_{1\text{-}p}$, were used to define a two-site model with a Hamiltonian given by $H = H_{1-p} + H_U$ where the Coulomb interactions, H_U, were defined in the spherically symmetric approximation according to the Slater parameters F_0, F_2 and F_4 (ref. [50]). For this purpose, we use the Hubbard repulsion $U_{t_{2g}} = 2.58$ and Hund's coupling $J_{t_{2g}} = 0.29$ eV following ref. [51], and approximate $F_4/F_2 = 5/8$ (ref. [52]). This corresponds to $F_0 = 2.15$ eV, $F_2 = 3.24$ eV and $F_4 = 2.02$ eV. After exactly diagonalizing the two-site model, we extract the magnetic couplings by projecting onto pure $J_{eff} = 1/2$ doublets of the ideal d^5 ground state.

The g-tensors. In order to estimate the magnetic g-tensors, we employed the method outlined in ref. [53]. From the structures employed in the calculation of the magnetic interactions, we extracted the coordinates of a single $[RuCl_6]^{3-}$ octahedron. For each, we computed the g-tensors using ORCA (ref. [54]) at the def2-SVP/PBEO/CAS-SCF(3,5) level. This approach has proved reliable in previous studies of $RuCl_3$ and other materials, and is consistent with expected trends.

Density functional theory structural relaxation. Our structural relaxation calculation of monolayer α-$RuCl_3$ was based on spin-polarized density functional theory as implemented in Vienna Ab-initio Simulation Package code[55] with a generalized gradient approximated exchange–correlation functional. The interaction between ion cores and valence electrons was described by a pseudopotential of projector augmented-wave type. A correction due to van der Waals forces was included through the DFT-D2 scheme of Grimme[56]. A plane-wave cut-off of 600 eV was used for the 2 × 2 supercell in the

slab geometry with 3 × 3 × 1 *k*-point sampling. The in-plane lattice parameters ($a = b = 12.00$ Å for 2 × 2 supercell) were chosen based on the electron diffraction results. A minimum distance of 9 Å was kept between two periodic images along the *c* direction.

Data availability

All relevant data within the article and supporting information are available from the corresponding authors upon reasonable request.

References

48. Riedl, K., Li, Y., Valentí, R. & Winter, S. M. Ab initio approaches for low-energy spin Hamiltonians. *Phys. Status Solidi* **256**, 1800684 (2019).
49. Eschrig, H., Richter, M. & Opahle, I. Relativistic solid state calculations. *Theor. Comput. Chem.* **14**, 723–776 (2004).
50. Sugano, S. *Multiplets of Transition-Metal Ions in Crystals* (Elsevier, 2012).
51. Eichstaedt, C. et al. Deriving models for the Kitaev spin-liquid candidate material *α*–$RuCl_3$ from first principles. *Phys. Rev. B* **100**, 075110 (2019).
52. Pavarini, E., Koch, E., Vollhardt, D. & Lichtenstein, A. *DMFT at 25: Infinite Dimensions* (Forschungszentrum Jülich, 2014).
53. Pedersen, K. S. et al. Iridates from the molecular side. *Nat. Commun.* **7**, 12195 (2016).
54. Neese, F. Software update: the ORCA program system, version 4.0. *Wiley Interdiscip. Rev. Comput. Mol. Sci.* **8**, e1327 (2018).
55. Kresse, G. & Hafner, J. *Ab initio* molecular dynamics for liquid metals. *Phys. Rev. B* **47**, 558–561 (1993).
56. Grimme, S. Semiempirical GGA-type density functional constructed with a long-range dispersion correction. *J. Comput. Chem.* **27**, 1787–1799 (2006).

Acknowledgements

A.W.T. acknowledges support from the US Army Research Office (W911NF-21-2-0136), Ontario Early Researcher Award (ER17-13-199) and the National Science and Engineering Research Council of Canada (RGPIN-2017-03815). This research was undertaken thanks in part to funding from the Canada First Research Excellence Fund. R. Hovden acknowledges support from the US Army Research Office (W911NF-22-1-0056), S.H.S. and Y.M.G. acknowledge support from the Keck Foundation. S.M.W. was supported by a pilot grant from the Center for Functional Materials, and performed computations on the Wake Forest University DEAC Cluster, a centrally managed resource with support provided in part by Wake Forest University. D.A.S.K., S.B. and R.V. acknowledge support by the Deutsche Forschungsgemeinschaft through grants VA 1171/15-1 and TRR 288-4 22213477 (project A05). G.Y. and R. He are supported by National Science Foundation CAREER grant no. DMR-1760668 and National Science Foundation grant no. DMR-2104036. H.L. acknowledges support by the National Key R&D Program of China (grant no. 2018YFE0202600), the Beijing Natural Science Foundation (grant no. Z200005) and the Fundamental Research Funds for the Central Universities and the Research Funds of Renmin University of China (18XNLG14 and 19XNLG17, respectively).

Author contributions

B.Y. and A.W.T. conceived and initiated the study. B.Y. fabricated the α-$RuCl_3$ devices for transport measurements, electron diffraction and Raman spectroscopy. B.Y. performed the IETS and lateral transport measurements. S.H.S., Y.M.G. and R. Hovden conducted the three-dimensional electron diffraction measurements. G.Y. and R. He performed the Raman spectroscopy. S.B., D.A.S.K., R.D., R.V. and S.M.W. performed the ab initio calculations. C.L., S.Y. and H.L. grew the α-$RuCl_3$ crystals. F.C. grew the 1T′-$MoTe_2$ crystals. S.J. conducted the magnetic circular dichroism measurements. B.Y. and A.W.T. wrote the manuscript with the input of all authors.

Competing interests

The authors declare no competing interests.

Additional information

Extended data is available for this paper at https://doi.org/10.1038/s41563-022-01401-3.

Supplementary information The online version contains supplementary material available at https://doi.org/10.1038/s41563-022-01401-3.

Correspondence and requests for materials should be addressed to Stephen M. Winter, Robert Hovden or Adam W. Tsen.

Peer review information *Nature Materials* thanks Hu Miao and the other, anonymous, reviewer(s) for their contribution to the peer review of this work.

https://doi.org/10.1038/s41563-022-01401-3

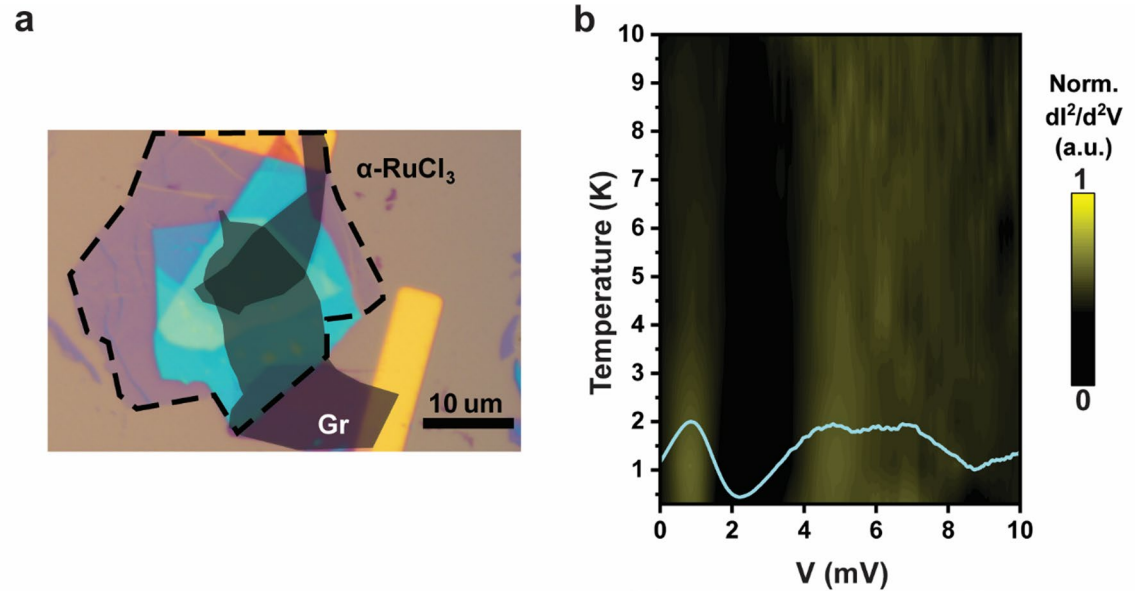

Extended Data Fig. 1 | IETS device with Gr contacts. (a): Colorized optical image of the sample. The device is fabricated in the same geometry as shown in Fig. 1a, except the T_d-$MoTe_2$ is replaced by few-layer graphene and the thickness of α-$RuCl_3$ is 5-6 layers. **(b)**: False-color two-dimensional plot of background-subtracted d^2I/dV^2 spectrum taken from 0.3 K to 10 K for positive bias. The trace at 0.3 K is overlaid in blue. The low-energy peak at 1 meV is reproduced in this sample, which gradually disappears above ~8 K, and the continuum between 4-10 meV is reproduced as well.

https://doi.org/10.1038/s41563-022-01401-3

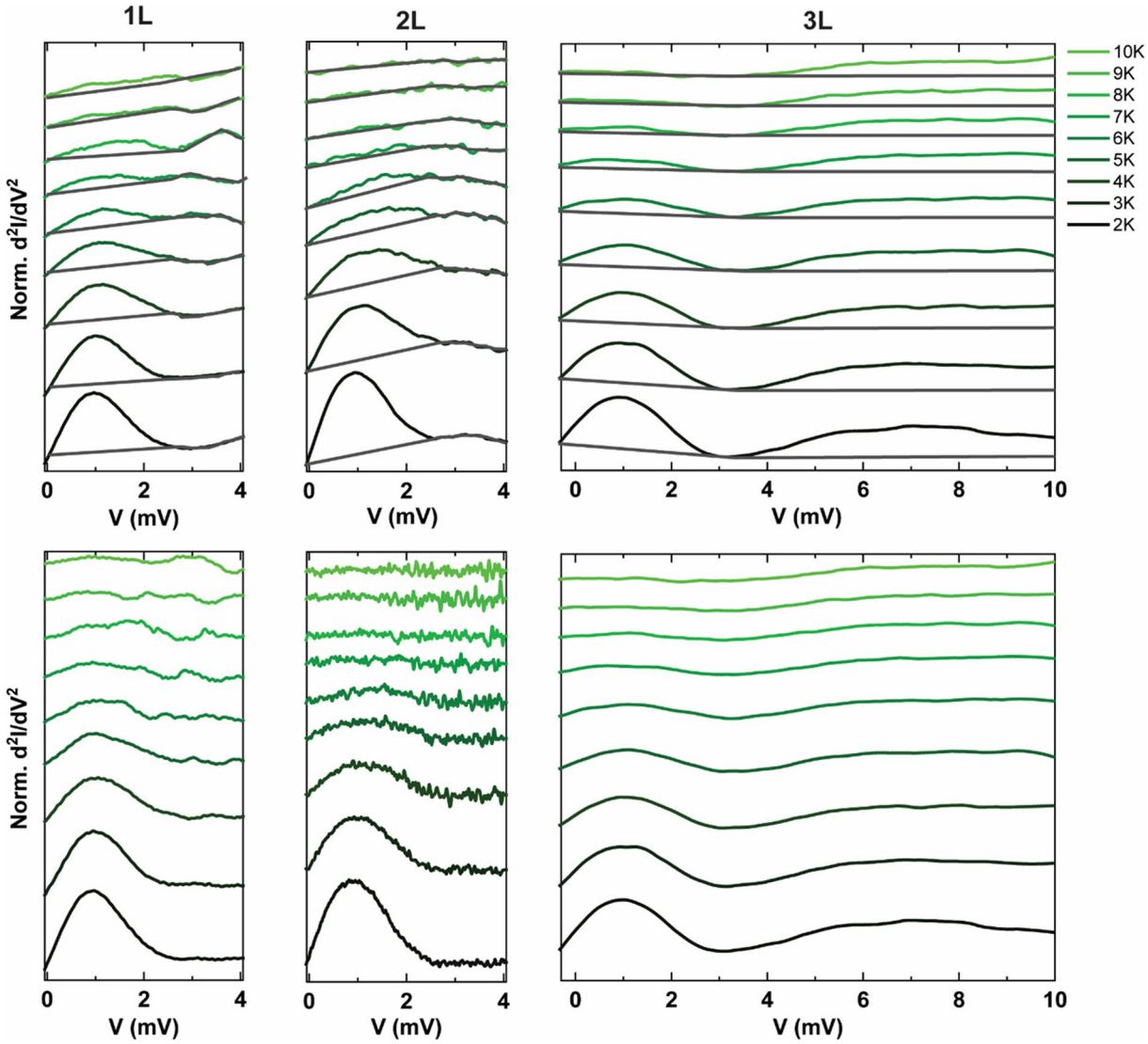

Extended Data Fig. 2 | Temperature-dependent IETS data on few-layer α-$RuCl_3$. Upper panels: 1L, 2L, and 3L α-$RuCl_3$ spectra with changing temperature from 2 K to 10 K in 1 K increments without background subtraction. Offset is applied for clarity. Grey lines represent the backgrounds for the IETS data. Lower panels: 1L, 2L, and 3L α-$RuCl_3$ spectra with background subtraction. The background-subtracted data is used for plotting Fig. 2.

https://doi.org/10.1038/s41563-022-01401-3

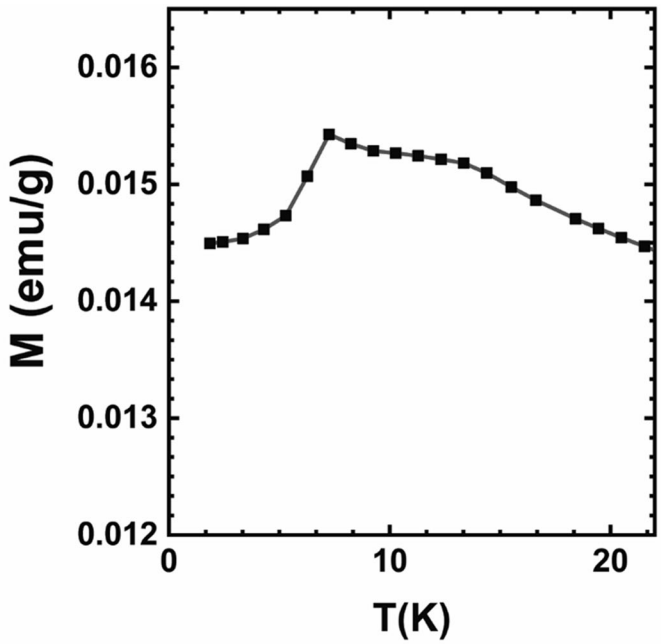

Extended Data Fig. 3 | Temperature dependence of magnetization for a bulk α-$RuCl_3$ single crystal used in the measurements. The sharp kink near 8 K indicates the Néel temperature, which is consistent with IETS data.

https://doi.org/10.1038/s41563-022-01401-3

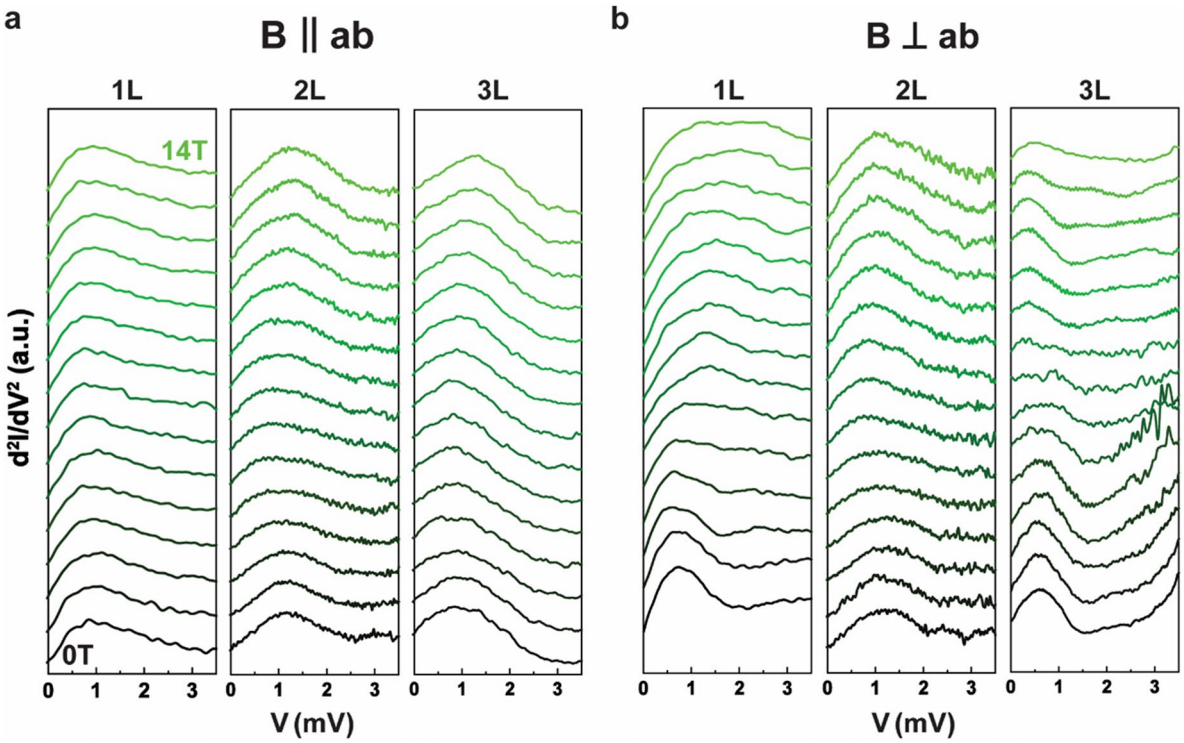

Extended Data Fig. 4 | Original field-dependent IETS data without background subtraction. 1L, 2L, and 3L α-$RuCl_3$ spectra without background subtraction with changing $B_{||}$ **(a)** and $B_{\perp}$ **(b)** from 0 T to 14 T in 1 T increments and offset for clarity.

https://doi.org/10.1038/s41563-022-01401-3

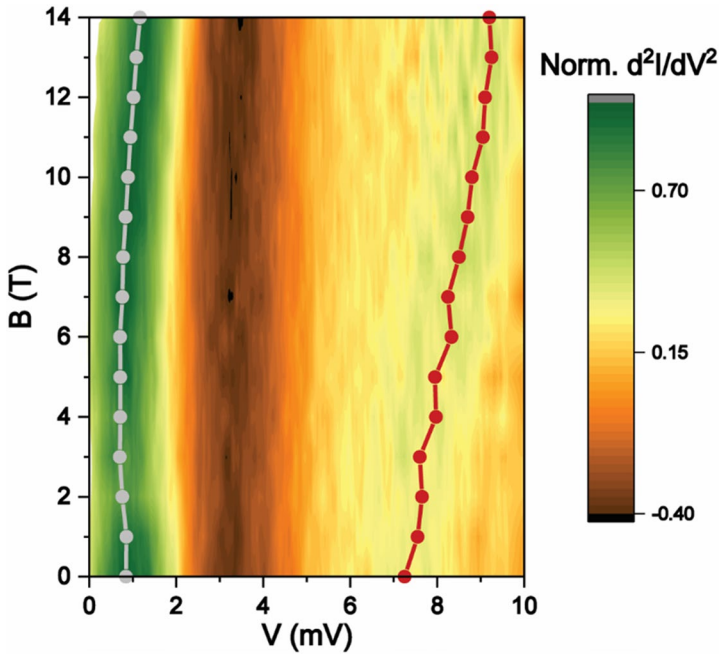

Extended Data Fig. 5 | False-color plot of normalized IETS spectra without background subtraction for 3L α-$RuCl_3$ from 0 T to 14 T. Evolution of the low-energy magnon peak and the maximum position of the magnon continuum is overlaid in grey and red, respectively.

https://doi.org/10.1038/s41563-022-01401-3

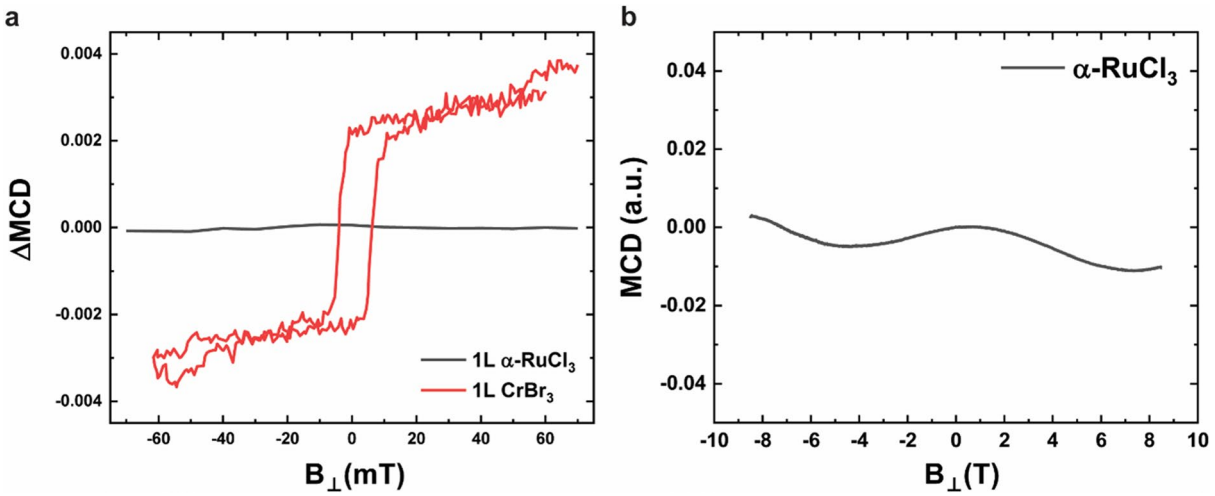

Extended Data Fig. 6 | Magnetic circular dichroism (MCD) measurements comparing 1L α-$RuCl_3$ and 1L $CrBr_3$. **(a)**: $\Delta MCD = \mathrm{MCD} - \mathrm{MCD}(0\mathrm{T})$ for 1L α-$RuCl_3$ at 3.5 K and 1L $CrBr_3$ at 5 K between ±70 mT. The data for 1L $CrBr_3$ is reproduced from previous work in ref. [27]. **(b)**: MCD data for 1L α-$RuCl_3$ at 3.5 K between ± 8 T.